ACS APPLIED MATERIALS & INTERFACES

www.acsami.org

Research Article

Thermochemical Mechanism of Optimized Lanthanum Chromite Heaters for High-Pressure and High-Temperature Experiments

Tao Xia, Yifeng Han, Chuanhui Zhu, Zhongxiong Sun, Chongyang Yuan, Qi Cui, Jin-Guang Cheng, Wei Du, Wenting Li, Kui Xie, Keke Huang, Shouhua Feng, David Walker,* and Man-Rong Li*

Cite This: *ACS Appl. Mater. Interfaces* 2022, 14, 32244−32252

Read Online

ACCESS | Metrics & More | Article Recommendations | Supporting Information

ABSTRACT: High-pressure heaters in large volume presses must reconcile potentially contradictory properties, and the whole high-pressure and high-temperature (HPHT) community has been engaged for years to seek a better heater. $LaCrO_3$ (LCO)-based ceramic heaters have been widely applied in multianvil apparatus; however, their performance is far from satisfactory, motivating further research on the chemical optimization strategy and corresponding thermochemical mechanism. Here, we adopted a chemical-screening strategy and manufactured tubular heaters using the electrically, chemically, and mechanically optimized Sr−Cu codoped $La_{0.9}Sr_{0.1}Cr_{0.8}Cu_{0.2}O_{3-\delta}$ (LSCCuO-9182). HPHT examinations of cylindrical LSCCuO-9182 heaters on Walker-type multianvil apparatuses demonstrated a small temperature gradient, robust thermochemical stability, and excellent compatibility with high-pressure assemblies below 2273 K and 10 GPa. Thermochemical mechanism analysis revealed that the temperature limitation of the LSCCuO-9182 heater was related to the autoredox process of the Cu dopant and Cr and the exchanging ionic migration of Cu and Mg between the LSCCuO-9182 heater and the MgO sleeve. Our combinatorial strategy coupled with thermochemical mechanism analysis makes the prioritization of contradictory objectives more rational, yields reliable LCO heaters, and sheds light on further improvement of the temperature limitation and thermochemical stability.

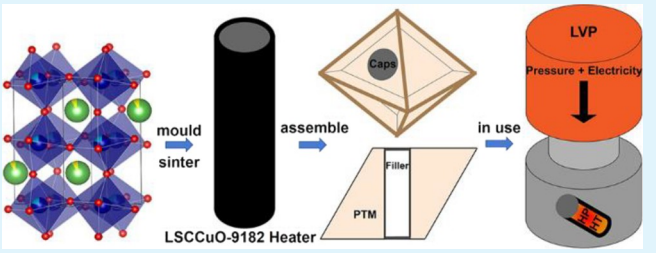

KEYWORDS: *high-pressure and high-temperature synthesis, $LaCrO_3$ ceramic heater, thermochemical mechanism, temperature field, high-pressure cell compatibility*

1. INTRODUCTION

Large volume presses (LVP) have been widely applied for high-pressure and high-temperature (HPHT) experiments to simulate the uppermost lower mantle conditions,[1−3] which are significant for new discoveries in interdisciplinary sciences.[4−8] Technological advancement in LVPs has been focused on the extension of the pressure and temperature limits under maximized space of the reaction chamber since the invention of multianvil apparatus.[9,10] To meet this end, the development of an appropriate heater is a prerequisite. An ideal resistive heater, such as a tubular-shaped one in the Walker-type multianvil press, is expected to offer sufficient conductivity, excellent thermochemical stability, strong refractoriness, acceptable mechanical strength, reasonable heat-retaining capability, a small temperature gradient, and considerable inertness against main components of the high-pressure cell over a wide pressure and temperature region.[11] In addition, easy fabrication (machinable) and cheapness should also be taken into account for the nominated candidates. Various heating schemes have been studied mainly in two categories, namely, metallic and ceramic-based heaters. Rhenium (Re) metal has been widely used to generate temperature up to 2923 K at high pressure (above 10 GPa).[12,13] Although considerable thermochemical stability can be achieved, the Re-heater is expensive and demonstrates poor heat-retaining performance and large axial and radial temperature drops. The graphite-based heater is cheap, easy to machine, and X-ray transparent and shows excellent thermochemical stability, good reproducibility of the heating efficiency, and an acceptable temperature gradient below 1773 K. However, a sufficiently long tubular graphite heater shape is unfavorable to avoid contact and corrosion of the tungsten carbide (WC) truncated cubes, which significantly decreases the specimen volume and shortens the length of the homogeneous temperature area. Moreover, a graphite heater undergoes a phase transition to insulating diamond at higher pressure and temperature.[14] Boron-doped diamond seems promising, but the heater fabrication requires a stringent and costly procedure.[15−17] In contrast, the relatively affordable lanthanum chromite

Received: April 30, 2022
Accepted: June 27, 2022
Published: July 6, 2022

Table 1. Experimental Conditions in Different HPHT Runs

run no.	octahedron	P/GPa	T/K	time	TC	cell	lab
HP0489	12 mm-646	3	1723	7 min	W/Re(C)	II	SYSU
			1773	7 min			
			1823	9 min			
HP0599	12 mm-646	5	1373	30 min	W/Re(C)	III	SYSU
HP0627	8 mm-646	8	1523	7 min	W/Re(C)	III	SYSU
HP222021	8 mm-584	10	1773	30 min	Pt/Rh (R)	II	IoP-CAS
BB1457	8 mm-646	4	1673	15 h	W/Re(D)	II	LDEO
			2273	10 min			
BB1437	12 mm-646	3	2073	30 min	W/Re(D)	I	LDEO
			2262	2 min			

($LaCrO_3$, hereafter denoted as LCO) based heater with a reasonable wall thickness is an excellent thermal insulator to trap heat and a semiconductor to promote uniform power dissipation, resulting in homogeneous axial and radial temperature field to maximize the useful reaction volume.[12,13,18] Nevertheless, LCO-based heaters can be too resistive at lower temperature at the beginning of heating for the power system (high electrical current and low voltage) of most of multianvil high pressure apparati. Second, the heating efficiency of LCO heaters is less reproducible, so that a single power-temperature relationship diagram is not applicable, requiring that an internal thermocouple should be applied to monitor the temperature variation. Third, LCO ceramic powder is difficult to mold and sinter to precise shape. Thus, as summarized in Table S1 in the Supporting Information, none of the known heaters are perfect. Although the combination of metal and ceramic heaters can partially do the job, for instance, a tubular LCO heater outside a Re tube can combine the advantages of both. However, the assembly is complicated and not cost-effective. Therefore, considering the merits of modified LCO, optimization and development of LCO heaters are highly desired, especially for large-volume and temperature-sensitive experiments.

LCO is a refractory oxide with melting point around 2703 K.[19] It adopts a distorted ABO_3-type perovskite structure (orthorhombic *Pbnm*) at room temperature[20] and undergoes reversible phase transitions to rhombohedral (*R*-3*c*) at ∼533 K and to a cubic (*Pm*-3*m*) polymorph at ∼1273 K upon heating at ambient pressure.[21,22] The *Pbnm*-to-*R*-3*c* transition has also been observed upon pressing up to ∼4.5 GPa.[23,24] Undoped LCO is a *p*-type semiconductor and too resistive to be utilized as heaters for HPHT experiments in LVP.[25] Acceptor doping by divalent ions into the trivalent sites has been extensively applied to increase the conductivity of modified LCO (producing holes and/or narrowing the band gap), mainly by similar-size alkali earth ions (Sr^{2+} or Ca^{2+}) to replace La^{3+} and/or 3*d*-transition metal ions (Mn^{2+}, Fe^{2+}, Co^{2+}, Cu^{2+}) to take over Cr^{3+}.[25−27] Although the electrical conductivity of modified LCO has been remarkably enhanced, there is still no satisfactory ingredient to simultaneously meet such requirements: enough conductivity at room and low temperature, excellent thermochemical stability over a considerable wide pressure and temperature region, being easy to mold and sinter into a precise and regular shape, and compatibility with most of the rest high-pressure cells. The key point is to seek for optimum chemical space and unveil the thermochemical mechanism for desired integrated performance.

In this work, we extensively screened the chemical space for codoped modification of LCO and singled out the optimized candidate via thorough characterization of the structure and electrical conductivity, thermochemical stability, and goodness of sintering and fabrication. The manufactured cylindrical heaters by optimal Sr^{2+}−Cu^{2+} codoped LCO were further tested in Walker-type multianvil apparatuses up to 10 GPa and 2273 K in various high-pressure cell assemblies at different laboratories, showing excellent and practical applications in LVP for HPHT experiments. The thermochemical mechanism was also investigated to show the direction of further heater design and improvement.

2. EXPERIMENTAL SECTION

2.1. Synthesis and Heater Fabrication. $La_{1-x}A_xCr_{1-y}B_yO_{3-\delta}$ (*A* = Ca, Sr; *B* = Fe, Co, Cu, Cu/Fe; $x \le 0.3$, $y \le 0.4$) were prepared via a solid-state reaction using a stoichiometric mixture of La_2O_3 (99.9%, Aladdin, preheated at 1173 K overnight to purify before mixing), $CaCO_3$ (99.99%, Macklin), $SrCO_3$ (99.95%, Aladdin), Cr_2O_3 (99.9%, Macklin), Co_3O_4 (99.9%, Macklin), Fe_2O_3 (99.99%, Alfa Aesar), and CuO (99.9%, HWRK CHEM). The mixture was pelletized and heated in air at 1473 K for 20 h, with a heating rate of 5 K/min and cooling naturally. The relatively more conductive $La_{1-x}Sr_xCr_{1-y}Co_yO_{3-\delta}$ (LSCCoO) and $La_{1-x}Sr_xCr_{1-y}Cu_yO_{3-\delta}$ (LSCCuO) were chosen for detailed studies. $La_{0.9}Sr_{0.1}Cr_{0.8}Cu_{0.2}O_{3-\delta}$ (hereafter denoted as LSCCuO-9182) powder and fluid wax (AR, Aladdin) in a ratio of 1 g: 40 μL were well mixed before pressing into a cylindrical mold and demolded, and the as-made cylinder was heated at 1473−1673 K for 10 h to get a LSCCuO-9182 heater with relative density ∼66%.

2.2. Powder X-ray Diffraction (PXD) and Chemical Analyses. The products were initially characterized by laboratory PXD in a RIGAKU D-MAX diffractometer (2200 VPC, Cu Kα, λ = 1.5418 Å) for phase identification and purity examination. In situ variable-temperature (VT)-PXD data were collected in a RIGAKU D-MAX 2200 VPC over a 2θ range of 10°−70° from 323 to 1473 K for thermal stability examination and 10°−110° from 323 to 773 K with a diamond internal standard for phase transition analysis. X-ray photoelectron spectroscopy (XPS) was performed on an ESCALAB 250 X-ray photoelectron spectrometer using Al Kα X-rays as an excitation source. Synchrotron PXD (SPXD) data were collected on the beamline BL14B at the Shanghai Synchrotron Radiation Facility (SSRF, λ = 0.68956 Å). Refinements of the SPXD data were carried out via GSASII and Topas Academic *V*6.[28]

2.3. Electrical Conductivity Measurements. LSCCuO-9182 pellets with the relative densities around 96% for conductivity measurement were prepared using the following procedure: the precalcined powder was mixed with 5% polyvinyl alcohol solution as an organic binder before being pressed into pellets with a diameter of 60 mm and a thickness of 22 mm and finally densified under a cold isostatic pressure of 300 MPa. The obtained pellets were buried inside LSCCuO-9182 sacrificial powder and sintered at 1773 K for 20 h, with a heating rate of 5 K/min and cooling naturally. The estimated densities of the pellets were calculated by using the geometric sizes (diameters and thickness) and the masses of the pellets. The sintered

https://doi.org/10.1021/acsami.2c07639
ACS Appl. Mater. Interfaces 2022, 14, 32244−32252

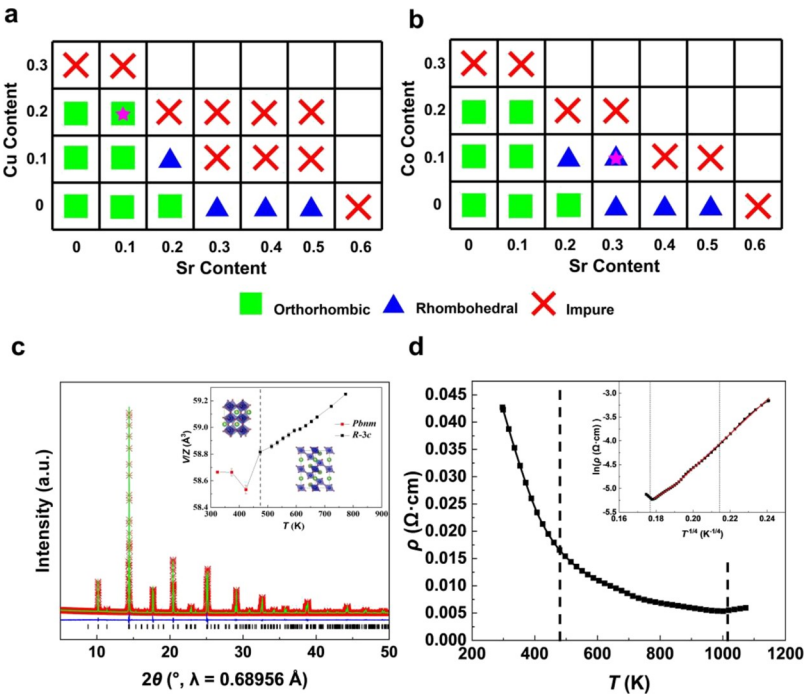

Figure 1. Phase diagram of (a) $La_{1-x}Sr_xCr_{1-y}Cu_yO_{3-\delta}$ and (b) $La_{1-x}Sr_xCr_{1-y}Co_yO_{3-\delta}$ ($x \leq 0.6$; $y \leq 0.3$). Phase information of $LaCr_{1-y}Cu_yO_3$ was extracted from reported work.[34] The purple stars highlight the composition with favorable conductivity used for heater fabrication discussed below. (c) Rietveld refinement of SPXD data for LSCCuO-9182. The red crosses represent the calculated fit, the green line the observed data, the deep blue line the difference, and black tick marks the peak positions. The inset shows the crystal structures (*Pbnm* and *R*-3*c*, La/Sr, green/yellow spheres; $(Cr/Cu)O_6$ octahedra, blue; O, red spheres.) and temperature-dependent volumetric evolution of LSCCuO-9182. The lattice parameters of LSCCuO-9182 at different temperatures were extracted from the in situ VT-PXD data. The dashed line indicates the *Pbnm* to *R*-3*c* phase transition boundary. (d) Temperature dependence of resistivity of LSCCuO-9182 bar in air under ambient pressure. Insets show the plots of lnρ versus $T^{-1/4}$.

LSCCuO-9182 pellets were cut into 1 × 1 × 13.3 mm bars for conductivity measurement. The resistivity of the samples was measured in air using a Keithley 2000 digital multimeter (Keithley Instruments Inc., USA), by the four-probe dc method between 297 and 1073 K recorded with a temperature step of 1 K.

2.4. Thermochemical Stability at HPHT. The fabricated heaters were examined in Walker-type multianvil presses up to 2273 K and 10 GPa. The ceramic octahedra used as pressure transmitting media (PTM) were cast using Aremco Ceramacast (ARMC) 646 (zirconia based)[9] and 584 (magnesia based),[1,2] respectively. C- or D-type W/Re and R-type Pt/Rh thermal couple junctions (Table 1) were adopted to monitor the temperature variation, respectively. Morphology and chemical mapping of the LSCCuO-9182 heaters before and after different runs were examined by optical microscopy and scanning electron microscopy (SEM, Thermo Fisher Scientific Phenom-Pharos FEG-SEM, using an accelerating voltage of 15 kV). The elemental distribution in different areas of the assemblies was examined by energy-dispersive X-ray spectroscopy equipped in the SEM and a JXA8230 electron probe microanalyzer (EPMA) with wavelength-dispersive spectrometers at the Institute of Geochemistry, Chinese Academy of Sciences, Guiyang, China. This instrument was operated at an accelerating voltage of 25 kV and a focused beam of 10 nA. The peak and background counting times were 30 s for peak and 15 s for La, Cr, Sr, Mg, and Zr, respectively, aside from Cu (10 and 5 s). Natural and synthetic standards were used for quantitative analyses: LaF_3 for La; cuprite for Cu; chromium for Cr, anhydrite for Sr; pyrope for Mg; cubic zirconia for Zr. All data were reduced with the ZAF (atomic number-absorption-fluorescence) procedure installed in the EPMA instruments. The detection limits are 0.03 wt% for La, 0.02 wt% for Cu, 0.05 wt% for Cr, 0.03 wt% for Sr, 0.01 wt% for Mg, and 0.02 wt% for Zr, respectively.

3. RESULTS AND DISCUSSION

3.1. Chemical Space Screening and Crystal Structure. In LCO, we tried codoping Sr or Ca on the La-site and Co, Fe, Cu, or Cu/Fe on the Cr-site, respectively, to compare the resistance (R) of different pellets made under the same conditions (1473 K, 12 h) for preliminary screening. As shown in Table S2, the Sr−Co and Sr−Cu mono- and codoping cases exhibit the most favorable electrical conductivity by initial check and are therefore chosen for further investigation. The dopant-dependent phase diagrams of $La_{1-x}Sr_xCr_{1-y}Cu_yO_{3-\delta}$ (LSCCuO) and $La_{1-x}Sr_xCr_{1-y}Co_yO_{3-\delta}$ (LSCCoO), originating from the room-temperature PXD patterns in Figure S1, are displayed in Figure 1a,b, where both systems undergo a phase transition from *Pbnm* to *R*-3*c* with the increase of Sr. In contrast, and mono-doping of Cu or Co at the Cr-site does not evoke any phase transition before an impurity appears. The *Pbnm*-to-*R*-3*c* transition boundary is around $x = 0.2$ and $y = 0.1$, while it tends to form the *R*-3*c* phase at $0.2 < x \leq 0.5$. Impurity phases (La_2CuO_4 and $SrCrO_4$) arise in the codoped systems with $y > 0.1$.

As shown in Tables S2 and S3, LSCCuO-9182 with $x = 0.1$ and $y = 0.2$ (highlighted in Figure 1a) and $La_{0.7}Sr_{0.3}Cr_{0.9}Co_{0.1}O_{3-\delta}$ (hereafter denoted as LSCCoO-7391 highlighted in Figure 1b) with $x = 0.3$ and $y = 0.1$ exhibit the best desired electrical conductivity. Figures 1c and S2 depict the Rietveld refinement results of the SPXD and PXD data for LSCCuO-9182 and LSCCoO-7391, in *Pbnm* and *R*-3*c*, respectively. The selected interatomic distances, bond angles, and observed bond valence sum calculations are listed in Tables S4, S5 and S6, S7 for LSCCuO-9182 and LSCCoO-

https://doi.org/10.1021/acsami.2c07639
ACS Appl. Mater. Interfaces 2022, 14, 32244−32252

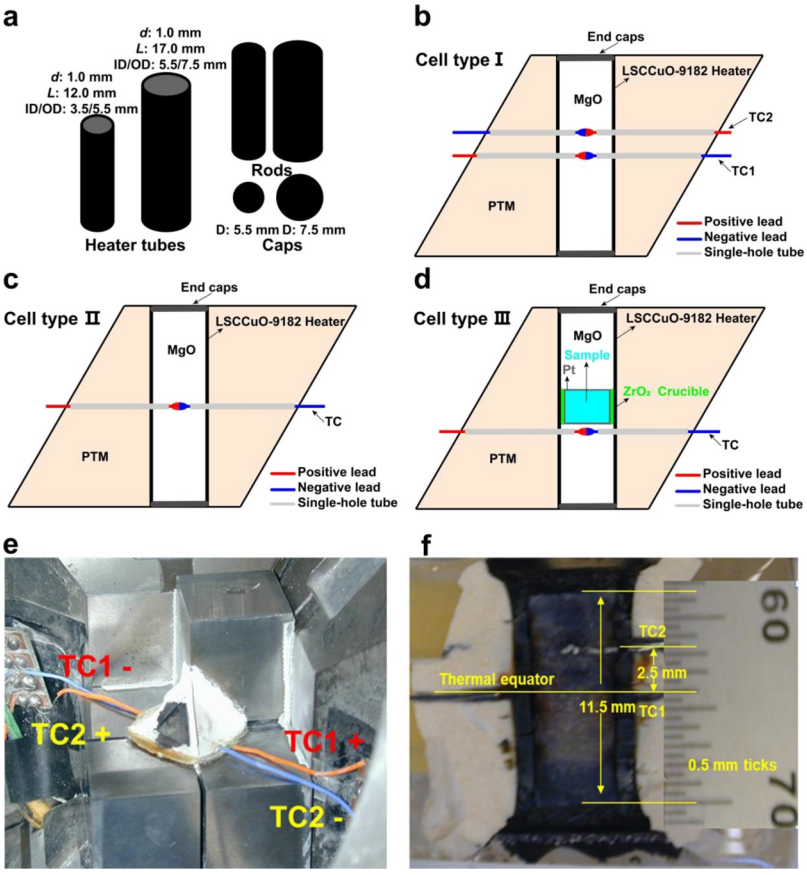

Figure 2. (a) Two types of LSCCuO-9182 heater tubes, rods and caps. (b) Schematic illustrations of a cross section of the cell assembly with two thermocouples (Cell type I). TC*n* (n = 1, 2) is for thermocouple label, the positive and negative electrodes are marked as "+" and "−" in Figure 2e, PTM is for pressure transmitting media of AREMCO-646 or 584. The MgO rods are applied as fillers. (c) Schematic illustrations of a cross section of the cell assembly with only one thermocouple (cell type II). (d) Schematic illustrations of a cross section of the cell assembly with only one thermocouple (cell type III). (e) Image of the high-pressure cell with two thermocouples. (f) Cross section of high-pressure cell of the HPHT run BB1437 at 3GPa up to 2262 K.

7391, respectively, which indicate the Cu^{+2} and Co^{+3} valence state in each. Although the Co- and Cu-modified LCO demonstrate comparable chemical and physical properties, subsequent ceramic processing shows that the Co version is very delicate and fragile, and difficult to machine. Therefore, we mainly focus on the Cu optimized LSCCuO-9182 for heater fabrication to understand the temperature dependence of heater performance.

3.2. Temperature-Dependent Structure and Conductivity at Ambient Pressure. Temperature-dependent phase transitions of LCO have been investigated by various diffraction methods, which indicates a transition from orthorhombic *Pbnm* to rhombohedral *R*-3*c* around 533 K accompanied by −0.138% volumetric expansion and to cubic *Pm*-3*m* around 1273 K.[21,22,29] In situ VT-PXD measurements at ambient pressure were performed to investigate the phase evolution of selected LSCCuO-9182 (Figures S3 and S4). LSCCuO-9182 exhibits excellent thermal and chemical stability up to 1473 K under experimental conditions. Upon heating to 473 K (Figure S4), a hexagonal (018) diffraction peak appears at ∼58.9°. The temperature-dependent volumetric evolution is shown in the inset of Figure 1c. Above 473 K, LSCCuO-9182 follows linear positive thermal expansion.

The slightly upward ρ between 1000 and 1100 K in Figure 1d could be attributed to the *R*-3*c* to *Pm*-3*m* transition, which is around 200 K lower compared to that in LCO.[21,22,29] The dimension change and corresponding possible ρ variation may trigger experimental failure (temperature hopping and/or blow-out) during HPHT experiments. Obviously, Sr−Cu codoping in LCO drives the phase transitions to lower temperatures, which is advantageous because any possible phase transition, accompanied by ρ change and temperature hopping, if there is any, occurring in a lower temperature region is more controllable and less harmful for HPHT operation. The ρ value of LSCCuO-9182 reads ∼0.042 and 0.005 Ω cm at room temperature and 1073 K, respectively, in Figure 1d, showing electronic conduction at lower temperature, and mixed electronic, hole, and defect (oxygen vacancy) conduction at higher temperature. The $\ln\rho - T^{-1/n}$ plot roughly follows a linear fitting for n = 4 in a higher temperature region (Figure 1d inset), suggesting three-dimensional Mott's variable-range-hopping-dominated transport mechanism.[30] According to previous reports, the LCO-based materials also tend to form a *R*-3*c* phase at room temperature under higher pressure (above 4.5 GPa).[23,24] The occurrence of *Pbnm*-to-*R*-3*c* transition upon pressing to ∼4.5 GPa at room temperature says that the above phase transition is accomplished before heating at higher pressure, which could result in stable HPHT experiments.

3.3. Heater Fabrication and Heating Performance at HPHT. Benefiting from codoping of *A* site-Sr and *B* site-Cu, the *Pbnm*-to-*R*-3*c* phase transition temperature of LCO is

https://doi.org/10.1021/acsami.2c07639
ACS Appl. Mater. Interfaces 2022, 14, 32244−32252

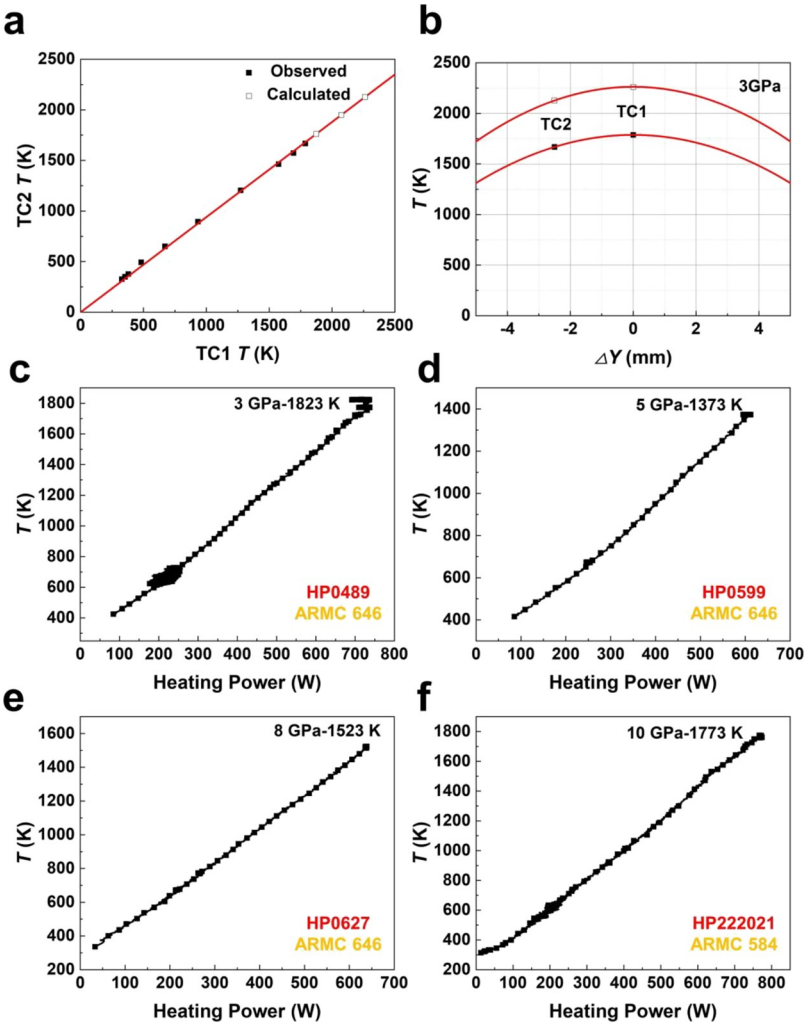

Figure 3. (a) TC1 and TC2 temperature in the BB1437 run. Calculated dots indicate the trend extension after the TC2 disconnection, the fitting curve is shown by red line. (b) Temperature profile with low gradients along the axial direction in the heater of BB1437 run. Diagrams of temperature versus heating power under different pressure at (c) 3 GPa, (d) 5 GPa, (e) 8 GPa, and (f) 10 GPa.

suppressed from 533 to 473 K at ambient pressure compared with that of pure LCO. LSCCuO-9182 is a pseudocubic phase at 1173 K and a cubic polymorph at 1473 K (Figures S3 and S4) as revealed by temperature-dependent phase analysis. Temperature-dependent four-probe dc conductivity measurements (Figure 1d) on LSCCuO-9182 at ambient pressure show no obvious resistivity (ρ) variation around the phase transition temperatures, suggesting negligible power (temperature) jumping for the HPHT process. Thereby, the as-made LSCCuO-9182 powder was first ball-milled to get a homogeneous and superfine particle size before mixing with an appropriate amount of fluid wax for heater fabrication. Two types of tubular heaters (Figure 2a) were molded according to the high-pressure assemblies for different target pressures: one with an inside diameter (ID) of 5.5 mm and length (L) of 17.0 mm (ϕ5.5/L17.0), and the other with ID/L = 3.5/12.0 mm (ϕ3.5/L12.0). The optimal wall thickness (d) of these heaters was controlled to be around 1 mm. Caps cut from sintered LSCCuO-9182 cylindrical rods, which were machined to have the same diameters as those of the outside diameter (OD) of heaters, were applied as electrodes (Figure 2a). We conducted a series of HPHT experiments using as-made LSCCuO-9182 heaters at 3−5 GPa (ϕ5.5/L17.0 heater) and 8−10 GPa (ϕ3.5/L12.0 heater) up to 2273 K as summarized in Table 1. Three types of high-pressure cells were applied for various purposes in our HPHT runs as shown in Figure 2b−d.

3.3.1. Temperature Gradient at 3 GPa. The performance of fabricated LSCCuO-9182 heaters was initially examined in a Walker-type multianvil apparatus in Lamont Doherty Earth Observatory (LDEO) at Columbia University, with a 12 mm truncation edge length (TEL) 646 octahedral cell on 27 mm FC3M cubes loaded to 250 tons (~3 GPa, cell type I in Figure 2e).[9] The run number is BB1437. A cross section of the recovered cell assembly is shown in Figure 2f. Two type-D W/Re thermal couple (TC, W3Re and W25Re) junctions were applied through the ϕ5.5/L17.0 heater insulated by single-hole MgO tubes at both sides. TC1 was at the thermal equator and TC2 was about 2.5 mm off the hot spot to monitor the axial temperature gradient. The remaining space inside the heater was filled by MgO rods. We also tried BN rods but they reacted with the heater and caused experimental failure (Figure S5). BB1437 was stably held at 2073 K for 30 min and then climbed to 2262 K, where it stayed for 2 min before an uncontrollable failure. TC2 ceased to work above 1800 K for an unknown reason. The observed temperature between TC1 and TC2 thermocouples is less than 100 K at 1273 K, 120 K at

https://doi.org/10.1021/acsami.2c07639
ACS Appl. Mater. Interfaces 2022, 14, 32244−32252

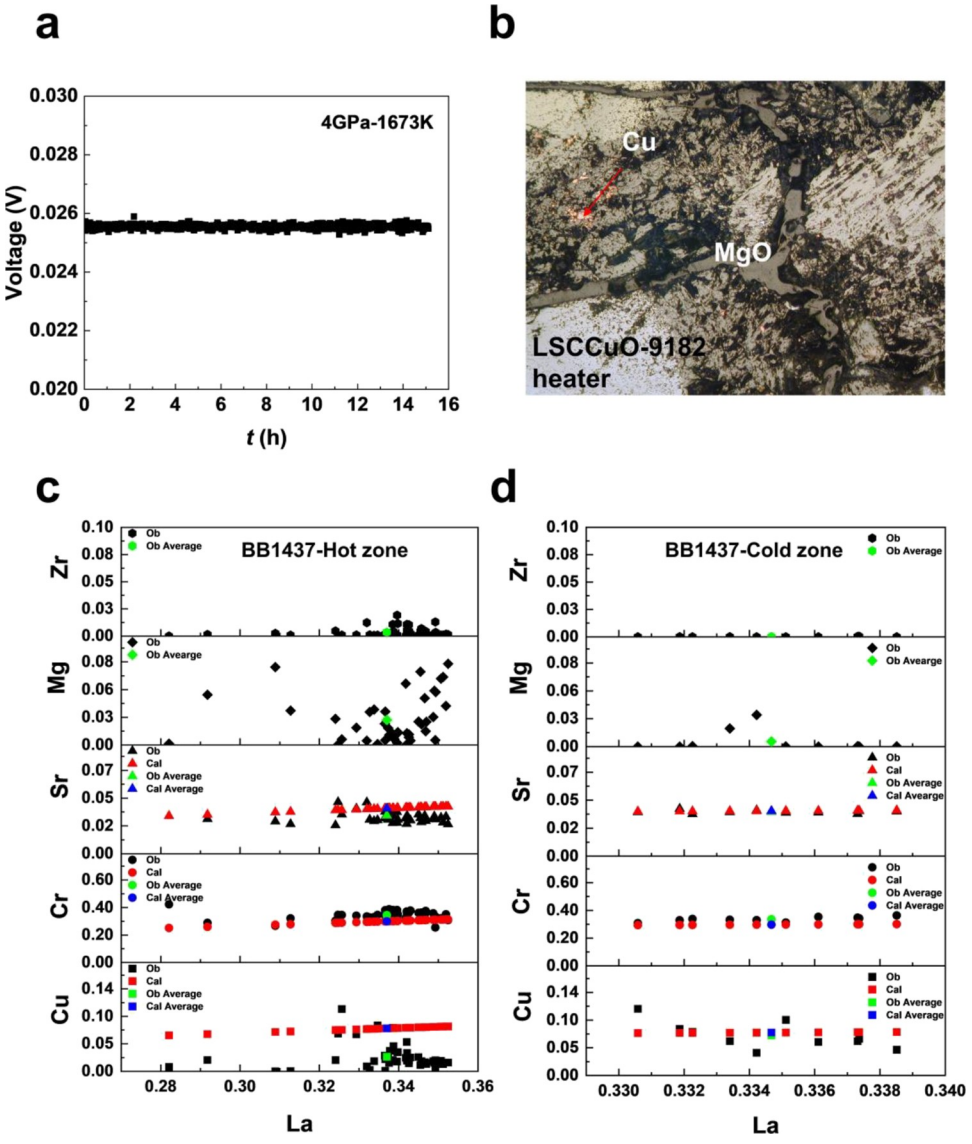

Figure 4. (a) Thermocouple voltage versus *t* of LSCCuO-9182 heater at 1673 K under 4 GPa (BB1457). (b) Image of the junction between MgO and the LSCCuO-9182 heater after HPHT BB1457. The elemental distribution of the LSCCuO-9182 heater after BB1437 run. (c) Hot zone part. (d) Cold zone part. "Ob" and "Cal" represent the observed and nominal values, respectively.

1773 K, and 135 K at 2262 K (Figure 3a). The temperature gradient in Figure 3b is substantially flatter than graphite and metal heaters, indicating the length of the homogeneous temperature-field zone is around 4−5 mm inside the heater.

Figure S6 gives the power and voltage versus temperature profiles of BB1437 recorded during the heating process. At low temperatures, approximately 50% power and 75 V were required to activate and heat the LSCCuO-9182 heater to 473 K. The *R* value rapidly decreased with increasing temperature. After passing the activation point, the resistance *R* was reduced more rapidly. The excursions marked by the rectangle were attributed to dopant redistribution around 673 K for half an hour. Above 673 K, there was no significant linear relationship between voltage/power and temperature, especially for power because tiny increase in power would cause a large increase in temperature. The temperature rose from 673 to 2262 K when the power increased from 49.5 to 57.4%. Therefore, temperature control of the LSCCuO-9182 heater by power is managed with difficulty, in contrast to metal or graphite heaters.

3.3.2. Heating Performance between 3 and 10 GPa in Different PTM. To further evaluate the performance of our heaters, more HPHT experiments were carried out using cell type-II and III (Figure 2c,d) between 3−10 GPa and 1373−1823 K (Table 1). The runs below and above 5 GPa were conducted by ϕ5.5/*L*17.0 and ϕ3.5/*L*12.0 heaters, respectively. For 3 (HP0489), 5 (HP0599), and 8 GPa (HP0627) runs at Sun Yat-Sen University (SYSU), the 646 octahedral cells were used with type-C W/Re thermocouples, while a 584 octahedral cell was applied with the R-type Pt/Rh thermocouple for the 10 GPa run (HP222021) at the Institute of Physics, Chinese Academy of Sciences (IoP-CAS). For comparison, the relationship between temperature and applied electrical power/heating resistance is shown in Figures 3c−f and S7. The high-pressure cell was held at 673 K for half an hour in each run, which caused a breakpoint in Figure S7. Our LSCCuO-9182 heaters demonstrated stable thermochemical behavior and excellent reproducibility up to 10 GPa and 1823 K in both 646- and 584-based PTMs. Figure S8 presented the PXD patterns of the cold (top) and hot (middle) sides of the

https://doi.org/10.1021/acsami.2c07639
ACS Appl. Mater. Interfaces 2022, 14, 32244−32252

heater after HP222021 run, indicating that the LSCCuO-9182-based heater remained stable after the HPHT experiment, and no distinct decomposition and/or phase separation occurred under the above experimental conditions.

Considering that application scenarios require long heating time, long-term stability of our heater was examined in a Walker-type multianvil apparatus with a 8 mm TEL 646 octahedral cell in BB1457 run at LDEO, where the type-II cell was heated at 1673 K under 4 GPa for a prolonged period of time to directly assess long-term stability. As shown in Figure 4a, the heater remained stable throughout the experiment at 1673 K for 15 h in the BB1457 run, during which the supply voltage on the thermocouple exhibited a tiny drift at 0.02552 ± 0.00024 V, suggesting excellent thermochemical stability of the LSCCuO-9182 heater under experimental conditions. Attempts to check the long-term stability at 2273 K were unsuccessful in BB1457 run, because the heating behavior became unstable and failed after 10 min.

3.4. Thermochemical Mechanism and Compatibility with High-Pressure Cell Assemblies. Optical microscope examination of the cross section of BB1457 cell after decompression displays some bubbled area with a free Cu metal phase (Figure 4b), probably due to local Cu-ion aggregation and thus melting of the Cu-rich area, which could be responsible for the temperature and R fluctuation at elevated temperature. Understandably, the codoping of Sr−Cu into LCO significantly increases the conductivity, but the formation of the eutectic phase lowers the melting point of LSCCuO-9182 compared with LCO. There could be a deficit of Cu in the eutectic phase, which drives metallic state Cu by a possible $Cr^{+3} + Cu^{+2} \rightarrow Cr^{+6} + Cu$ redox reaction (Figure S9).[31] Alternately, the temperature limitation may in part be initiated by the CuO in solution in the LCO undergoing the autoreduction $CuO \rightarrow Cu + 1/2O_2$ which has a thermal equilibrium near 2000 K in the undiluted state.[32,33] The encounter of this autoreduction diluted in solution in the LCO will be governed by complex activity-composition relations. The T_{max}−P diagram (Figure S10) extracted from the profiles of these runs suggests that the heater can be stably run at 2273 K or higher temperature if the pressure increases, because the melting point of many materials rises at higher pressure.

Figure S8 represents the comparison of PXD patterns from the LSCCuO-9182 heater before and after the HP222021 run. Clearly, LSCCuO-9182 remains stable at 10 GPa and 1773 K. To further investigate the elemental distribution in the microscopic region of the heater and boundary area within the assemblies, high-resolution microprobe measurements were performed on BB1437 and BB1457 runs. Three different regions of the original heaters were selected for elemental analysis before HPHT experiments for reference as shown in Figures S11a and S12a,b, where all elements were close to the nominal stoichiometry. LSCCuO-9182 heaters after the HPHT measurements were divided as hot and cold zones as shown in Figures S11b and S11c for BB1437 and BB1457 runs, respectively. The La, Sr, and Cr elements were comparable to the stoichiometric ratios, while a significant decrease of Cu and a clear increase of Mg were observed in the hot zones of heaters as shown in Figures 4c and S13a. In contrast, at the cold zone, all elements remained in the same ratio as in the origin heater (Figures 4d and S13b). Such a difference in the Cu and Mg distribution clearly originated from the temperature difference between the hot and cold zones. A rational explanation is that some Cu migrates into the MgO rod, and Mg enters the heater at the hot end. To verify this hypothesis, the boundary areas with MgO rods (contacting with the inside heater wall) and PTM-646 (bonding with the outside heater wall) were also analyzed to trace the elemental migration. Microprobe measurements on the MgO rod near the inner-boundary (Figures S14a and S15a) showed significantly different contents of Cu and Mg at the cold and hot ends, where the cold zone contained more Cu and less Mg compared to the hot end, suggesting that Cu could migrate into the MgO rod at the hot zone and then diffuse to the cold side. In contrast, no elemental migration (Figures S14b and S15b) was found in the colder PTM-646 side, indicating that LSCCuO-9182 was inert enough to zirconia PTM under experimental conditions. Similar results were obtained for SEM results in the cell after HP222021 run (Figure S16). Therefore, it is conclusive that the Cu in the heater exchanges with Mg in the MgO rod above 1773 K.

Accordingly, we can conclude that considerable exchange migration of Cu−Mg ions between the heater and MgO rod occurred at 2273 K is undoubtedly partially responsible for the failure in BB1457 and BB1437 runs, while in the HP222021 run (10 GPa and 1773 K), the Mg−Cu exchange is hard to see in the hot zone (Figure S16c). The autoreduction of CuO in solution in LCO at T > 2000 K is also a possible contributory mechanism to heater failure at high T. Replacing the MgO filler (Figure 2b−d) inside the heater by others, such as ZrO_2 rods, may be beneficial to the stable HPHT runs at or above 2273 K, which will be examined in future tests. It is safe to apply MgO rods and PTM-584 below conservative low temperature (1773 K) in that HP222021 ran successfully.

4. CONCLUSIONS

Our chemical screening and optimization of $LaCrO_3$ reveal that Sr and Cu codoped $La_{0.9}Sr_{0.1}Cr_{0.8}Cu_{0.2}O_{3-\delta}$ (LSCCuO-9182) exhibits the most appealing conductivity, sinterability, and machinability. The heater fabricated by LSCCuO-9182 shows a small temperature gradient (large useful volume), excellent thermochemical stability, strong refractoriness, acceptable mechanical strength, and considerable compatibility with high-press cell in HPHT experiments up to 10 GPa and 2273 K, which were performed by different PTM in three different laboratories. The thermochemical mechanism analyses reveal that the Mg−Cu ion-exchange between the inner skin of heater and filled MgO rods leads to local phase separation, which together with small melted Cu domains from mysterious CuO autoreduction or Cr−Cu redox process is mainly responsible for the fluctuation of resistance and temperature above 2073 K. The as-made heaters are expected to be widely used in a wider pressure and temperature region for LVPs, where MgO and BN-free filler rods like ZrO_2 are highly favorable to extend the temperature limit for HPHT experiments. These findings develop a practical and optimized LaCrO3-based heater up to 2273 K for HPHT synthesis and guide a way to further extend the temperature limit.

■ ASSOCIATED CONTENT

Supporting Information

The Supporting Information is available free of charge at https://pubs.acs.org/doi/10.1021/acsami.2c07639.

Crystallographic information file for $La_{0.9}Sr_{0.1}Cr_{0.8}Cu_{0.2}O_3$ (CIF)

https://doi.org/10.1021/acsami.2c07639
ACS Appl. Mater. Interfaces 2022, 14, 32244−32252

PXD patterns for the series of compounds (Figures S1−16); VT-PXD patterns of LSCCuO-9182; PXD patterns of LSCCuO-9182 before and after HP222021; electrical parameters in different HPHT tests; XPS patterns of Cr_2O_3 and LSCCuO-9182 before and after BB1457; microprobe areas and elements ratio of LSCCuO-9182 before and after HPHT tests; mapping images of LSCCuO-9182 after HP222021; comparison of the different heaters; the resistance of the relevant materials; crystal structure refinement details (PDF)

AUTHOR INFORMATION

Corresponding Authors

David Walker − *Lamont Doherty Earth Observatory, Columbia University, Palisades, New York 10964, United States*; Email: dwalker@ldeo.columbia.edu

Man-Rong Li − *Key Laboratory of Bioinorganic and Synthetic Chemistry of Ministry of Education, School of Chemistry, Sun Yat-Sen University, Guangzhou 510275, P. R. China*; orcid.org/0000-0001-8424-9134; Email: limanrong@mail.sysu.edu.cn

Authors

Tao Xia − *Key Laboratory of Bioinorganic and Synthetic Chemistry of Ministry of Education, School of Chemistry, Sun Yat-Sen University, Guangzhou 510275, P. R. China*

Yifeng Han − *Key Laboratory of Bioinorganic and Synthetic Chemistry of Ministry of Education, School of Chemistry, Sun Yat-Sen University, Guangzhou 510275, P. R. China*

Chuanhui Zhu − *Key Laboratory of Bioinorganic and Synthetic Chemistry of Ministry of Education, School of Chemistry, Sun Yat-Sen University, Guangzhou 510275, P. R. China*

Zhongxiong Sun − *Key Laboratory of Bioinorganic and Synthetic Chemistry of Ministry of Education, School of Chemistry, Sun Yat-Sen University, Guangzhou 510275, P. R. China*

Chongyang Yuan − *Key Laboratory of Bioinorganic and Synthetic Chemistry of Ministry of Education, School of Chemistry, Sun Yat-Sen University, Guangzhou 510275, P. R. China*

Qi Cui − *Beijing National Laboratory for Condensed Matter Physics and Institute of Physics, Chinese Academy of Sciences, Beijing 100190, P. R. China*

Jin-Guang Cheng − *Beijing National Laboratory for Condensed Matter Physics and Institute of Physics, Chinese Academy of Sciences, Beijing 100190, P. R. China*; orcid.org/0000-0002-4969-1960

Wei Du − *State Key Laboratory of Ore Deposit Geochemistry, Institute of Geochemistry, Chinese Academy of Sciences, Guiyang 550081, P. R. China*

Wenting Li − *Key Laboratory of Design & Assembly of Functional Nanostructures, Fujian Institute of Research on the Structure of Matter, Chinese Academy of Sciences, Fuzhou 350002, P. R. China*

Kui Xie − *Key Laboratory of Design & Assembly of Functional Nanostructures, Fujian Institute of Research on the Structure of Matter, Chinese Academy of Sciences, Fuzhou 350002, P. R. China*; orcid.org/0000-0002-1215-0271

Keke Huang − *State Key Laboratory of Inorganic Synthesis and Preparative Chemistry, College of Chemistry, Jilin University, Changchun 130012, P. R. China*; orcid.org/0000-0002-8995-2176

Shouhua Feng − *State Key Laboratory of Inorganic Synthesis and Preparative Chemistry, College of Chemistry, Jilin University, Changchun 130012, P. R. China*

Complete contact information is available at: https://pubs.acs.org/10.1021/acsami.2c07639

Author Contributions

M.-R.L. and. D.W. designed the research; T.X., Y.H., C.Z., Z.S., and C.Y. performed the chemical screening, heater fabrication, and HPHT tests in PTM-646; Q.C. and J.G.C. conducted the HPHT tests in PTM-584; W.D. carried out microprobe and data analysis; W.L. and K.X. measured the temperature-dependent resistivity at ambient pressure; K.H. and S.F. conducted the XPS runs; D.W. performed the temperature-field and limitation tests. All the authors participated the paper writing. T.X. and Y.H. contributed equally.

Notes

The authors declare no competing financial interest.

ACKNOWLEDGMENTS

This work was financially supported by the National Natural Science Foundation of China (NSFC-22090041, 21875287, and 22105228). The authors thank Dr. J. Zhang at Shanghai Institute of Ceramics, the Chinese Academy of Sciences for initial heater fabrication test, beamline BL14B1 (SSRF) for providing the beam time.

REFERENCES

(1) Walker, D. Lubrication, gasketing, and precision in multianvil experiments. *Am. Miner.* **1991**, *76*, 1092−1100.

(2) Walker, D.; Carpenter, M. A.; Hitch, C. M. Some simplifications to multianvil devices for high pressure experiments. *Am. Miner.* **1990**, *75*, 1020−1028.

(3) Abelson, P. H. Experimental Technology. *Science* **1999**, *283*, 1263.

(4) Jin, F.; Wang, L.; Zhang, A.; Ji, J.; Shi, Y.; Wang, X.; Yu, R.; Zhang, J.; Plummer, E. W.; Zhang, Q. Raman interrogation of the ferroelectric phase transition in polar metal $LiOsO_3$. *Proc. Natl. Acad. Sci. U. S. A.* **2019**, *116*, 20322.

(5) Walker, D. *Plates, planets, and phase changes: 50 years of petrology*; Geological Society of America, 2013; Vol. *500*, pp 1−32.

(6) Duffy, T. Earth science: Crystallography's journey to the deep Earth. *Nature* **2014**, *506*, 3.

(7) Huppertz, H. New synthetic discoveries via high-pressure solid-state chemistry. *Chem. Commun.* **2011**, *47*, 131−140.

(8) Goodenough, J. B.; Kafalas, J. A.; Longo, J. M., High-Pressure Synthesis. In *Preparative Methods in Solid State Chemistry*; Hagenmuller, P., Ed.; Academic Press, 1972; pp 1−69.

(9) Walker, D.; Li, J. Castable solid pressure media for multianvil devices. *Matter Radiat. Extremes* **2019**, *5*, No. 018402.

(10) Liebermann, R. C. Multi-anvil, high pressure apparatus: a half-century of development and progress. *High Pressure Res.* **2011**, *31*, 493−532.

(11) Kanke, Y.; Akaishi, M.; Yamaoka, S.; Taniguchi, T. Heater cell for materials synthesis and crystal growth in the large volume high pressure apparatus at 10 GPa. *Rev. Sci. Instrum.* **2002**, *73*, 3268−3270.

(12) Ito, E.; Katsura, T., Melting of Ferromagnesian Silicates Under the Lower Mantle Conditions. In *High-Pressure Research: Application to Earth and Planetary Sciences*; Terra Scientific Publishing Company, 1992; pp 315−322.

(13) Zhang, J.; Liebermann, R. C.; Gasparik, T.; Herzberg, C. T.; Fei, Y. Melting and subsolidus relations of SiO_2 at 9−14 GPa. *J. Geophys. Res. Solid Earth* **1993**, *98*, 19785−19793.

(14) Borimsky, A. I.; Volkov, V. B.; Nagorny, P. A., High pressure cell heaters for diamond synthesis. In *High Pressure Chemical*

Engineering, Proceedings of the 3rd International Symposium on High Pressure Chemical Engineering; von Rohr, P. R.; Trepp, C., Eds.; Elsevier, 1996; Vol. *12*, pp 651−654.
(15) Yamada, A.; Irifune, T.; Sumiya, H.; Higo, Y.; Inoue, T.; Funakoshi, K.-I. Exploratory study of the new B-doped diamond heater at high pressure and temperature and its application to in situ XRD experiments on hydrous Mg-silicate melt. *High Pressure Res.* **2008**, *28*, 255−264.
(16) Shatskiy, A.; Yamazaki, D.; Morard, G.; Cooray, T.; Matsuzaki, T.; Higo, Y.; Funakoshi, K.-I.; Sumiya, H.; Ito, E.; Katsura, T. Boron-doped diamond heater and its application to large-volume, high-pressure, and high-temperature experiments. *Rev. Sci. Instrum.* **2009**, *80*, No. 023907.
(17) Bundy, F. P.; Bassett, W. A.; Weathers, M. S.; Hemley, R. J.; Mao, H. U.; Goncharov, A. F. The pressure-temperature phase and transformation diagram for carbon; updated through 1994. *Carbon* **1996**, *34*, 141−153.
(18) Andrianov, M. A.; Balkevich, V. L.; Sotnikov, V. E. Use of lanthanum chromite for making electric heaters. *Refract.* **1980**, *21*, 592−596.
(19) Ma, P.; Zhang, H.; Chen, M.; Liu, T.; Chang, A.; Su, Z. Highly dense $LaCrO_3$ ceramics fabricated in air ambient. *J. Mater. Sci.: Mater. Electron.* **2019**, *30*, 9983−9988.
(20) Bonet, A.; to Baben, M.; Travitzky, N.; Greil, P. High-Temperature Electrical Conductivity of $LaCr_{1-x}Co_xO_3$ Ceramics. *J. Am. Ceram. Soc.* **2016**, *99*, 917−921.
(21) Hashimoto, T.; Tsuzuki, N.; Kishi, A.; Takagi, K.; Tsuda, K.; Tanaka, M.; Oikawa, K.; Kamiyama, T.; Yoshida, K.; Tagawa, H.; Dokiya, M. Analysis of crystal structure and phase transition of $LaCrO_3$ by various diffraction measurements. *Solid State Ionics* **2000**, *132*, 181−188.
(22) Momin, A. C.; Mirza, E. B.; Mathews, M. D. High-temperature X-ray diffractometric studies of $LaCrO_3$. *J. Mater. Sci. Lett.* **1991**, *10*, 1246−1248.
(23) Li, N.; Zhang, Q.; Wang, Y.; Yang, W. Perspective on the pressure-driven evolution of the lattice and electronic structure in perovskite and double perovskite. *Appl. Phys. Lett.* **2020**, *117*, No. 080502.
(24) Bhadram, V. S.; Sen, A.; Sunil, J.; Panda, D. P.; Sundaresan, A.; Narayana, C. Pressure-driven evolution of structural distortions in $RCrO_3$ perovskites: The curious case of $LaCrO_3$. *Solid State Sci.* **2021**, *119*, No. 106708.
(25) Gupta, S.; Mahapatra, M. K.; Singh, P. Phase transformation, thermal expansion and electrical conductivity of lanthanum chromite. *Mater. Res. Bull.* **2013**, *48*, 3262−3267.
(26) Zhang, K. H. L.; Du, Y.; Papadogianni, A.; Bierwagen, O.; Sallis, S.; Piper, L. F. J.; Bowden, M. E.; Shutthanandan, V.; Sushko, P. V.; Chambers, S. A. Perovskite Sr-Doped $LaCrO_3$ as a New p-Type Transparent Conducting Oxide. *Adv. Mater.* **2015**, *27*, 5191−5195.
(27) Raffaelle, R.; Anderson, H. U.; Sparlin, D. M.; Parris, P. E. Evidence for a crossover from multiple trapping to percolation in the high-temperature electrical conductivity of Mn-doped $LaCrO_3$. *Phys. Rev. Lett.* **1990**, *65*, 1383−1386.
(28) Coelho, A. A. TOPAS and TOPAS-Academic: an optimization program integrating computer algebra and crystallographic objects written in C++. *J. Appl. Crystallogr.* **2018**, *51*, 210−218.
(29) Oikawa, K.; Kamiyama, T.; Hashimoto, T.; Shimojyo, Y.; Morii, Y. Structural Phase Transition of Orthorhombic $LaCrO_3$ Studied by Neutron Powder Diffraction. *J. Solid State Chem.* **2000**, *154*, 524−529.
(30) Mott, N. F. *Conduction in non-crystalline materials*, 2nd ed.; Clarendon Press: Oxford, 1993.
(31) Choudhary, B.; Paul, D.; Singh, A.; Gupta, T. Removal of hexavalent chromium upon interaction with biochar under acidic conditions: mechanistic insights and application. *Environ. Sci. Pollut. Res.* **2017**, *24*, 16786−16797.
(32) Kim, J. Y.; Rodriguez, J. A.; Hanson, J. C.; Frenkel, A. I.; Lee, P. L. Reduction of CuO and Cu_2O with H_2: H Embedding and Kinetic Effects in the Formation of Suboxides. *J. Am. Chem. Soc.* **2003**, *125*, 10684−10692.
(33) Rakita, Y.; O'Nolan, D.; McAuliffe, R. D.; Veith, G. M.; Chupas, P. J.; Billinge, S. J. L.; Chapman, K. W. Active Reaction Control of Cu Redox State Based on Real-Time Feedback from In Situ Synchrotron Measurements. *J. Am. Chem. Soc.* **2020**, *142*, 18758−18762.
(34) Qasim, I.; Blanchard, P. E.; Liu, S.; Kennedy, B. J.; Avdeev, M. Impact of Cu Doping on the Structure and Electronic Properties of $LaCr_{1-y}Cu_yO_3$. *Inorg. Chem.* **2014**, *53*, 2240−2247.

https://doi.org/10.1021/acsami.2c07639
ACS Appl. Mater. Interfaces 2022, 14, 32244−32252